Observation of Spin Splitting Torque in a Collinear Antiferromagnet RuO_2

H. Bai,[1,*] L. Han,[1,*] X. Y. Feng,[2,*] Y. J. Zhou,[1] R. X. Su,[1] Q. Wang,[1] L. Y. Liao,[1] W. X. Zhu,[1] X. Z. Chen,[1] F. Pan,[1] X. L. Fan,[2,†] and C. Song[1,‡]

[1]*Key Laboratory of Advanced Materials, School of Materials Science and Engineering, Tsinghua University, Beijing 100084, China*

[2]*The Key Lab for Magnetism and Magnetic Materials of Ministry of Education, Lanzhou University, Lanzhou 730000, China*

(Received 13 September 2021; revised 22 February 2022; accepted 15 April 2022; published 13 May 2022)

Current-induced spin torques provide efficient data writing approaches for magnetic memories. Recently, the spin splitting torque (SST) was theoretically predicted, which combines advantages of conventional spin transfer torque (STT) and spin-orbit torque (SOT) as well as enables controllable spin polarization. Here we provide the experimental evidence of SST in collinear antiferromagnet RuO_2 films. The spin current direction is found to be correlated to the crystal orientation of RuO_2 and the spin polarization direction is dependent on (parallel to) the Néel vector. These features are quite characteristic for the predicted SST. Our finding not only presents a new member for the spin torques besides traditional STT and SOT, but also proposes a promising spin source RuO_2 for spintronics.

DOI: 10.1103/PhysRevLett.128.197202

Current-induced spin torques not only enrich fundamental physics, but also provide efficient data writing approach for magnetic memories. The discovery of spin transfer torque (STT) brings about electrical switching of ferromagnetism, giving rise to the nonvolatile magnetic random-access memory (STT-MRAM) with high speed and low consumption [1–5]. The longitudinal spin polarized current for STT is odd under time reversal ($\mathcal{T}$) and has high spin torque efficiency, due to the strong nonrelativistic ferromagnetic exchange splitting [1,2,4]. In contrast, transversal spin current with $\mathcal{T}$ even can be generated via the relativistic spin Hall effect (SHE) or/and the Rashba effect [6–8], which decouples reading and writing paths in MRAM and improves the device endurance. The resultant spin-orbit torque (SOT) has been extensively studied in the last decade for SOT-MRAM [9,10].

Recently, a distinct spin splitting torque (SST) with the origin of nonrelativistic anisotropic spin band splitting was theoretically predicted in antiferromagnets [11–17]. In this scenario, transversal spin current with high spin torque efficiency is generated by the magnetic exchange splitting ($\mathcal{T}$ odd) and is independent on the spin-orbit coupling (SOC), which provides a unique opportunity to combine the advantages of STT and SOT. Meanwhile, SST shows the advantage of controllable spin polarization, which would expand the horizon of spin torque switching. For example, SST offers a different approach for generating out-of-plane spin polarization, and the efficiency is expected to be higher than other mechanisms relying on low crystal symmetry and magnetic ordering [18–21]. The experiments below provide evidence of the anisotropic spin splitting effect (ASSE) induced SST in a collinear antiferromagnet RuO_2, where the spin current direction is correlated to the crystal orientation and the spin polarization direction is dependent on the magnetic orientation, i.e., Néel vector of RuO_2.

RuO_2 was commonly considered as a paramagnet, until the recent finding of itinerant antiferromagnetism, with the Néel temperature above 300 K and the Néel vector aligned along the [001] axis [22,23]. The crystal and magnetic structure of RuO_2 is shown in Fig. 1(a). RuO_2 is a rutile oxide with the $P4_2/mnm$ space group, where Ru atoms occupy the center of stretched oxygen octahedrons [24]. Consequently, Ru atoms suffer from the octahedral crystal field, giving rise to anisotropic electronic structure and elliptical Fermi circles at $k_z = 0$ [12], as illustrated in Fig. 1(b). Note that Ru atoms of opposite magnetic sublattices are surrounded by different directional oxygen octahedrons (with 90° rotation). Such a sublattice rotation in real space results in anisotropic spin band splitting in momentum space [Fig. 1(b)], ensuring RuO_2 an efficient spin splitter to generate spin current. Two typical configurations to generate spin current were proposed in Ref. [12]. For the (100)-oriented RuO_2 film, charge current applied along the $[0\bar{1}0]$ axis can induce a transversal $\mathcal{T}$-odd spin current flowing along the [100] direction (out-of-plane), and the spin polarization direction is parallel to the Néel vector ([001] axis), as illustrated in Fig. 1(c). When the $RuO_2(100)$ film is adjacent to a ferromagnetic layer, the transversal spin current will induce the spin splitting torque. Differently, for the (110)-oriented RuO_2 film, charge current applied along the $[1\bar{1}0]$ axis produces only longitudinal spin polarized current, the transversal spin current is forbidden due to the symmetry, as displayed in Fig. 1(d) [25]. As a result, SST is absent for this case.

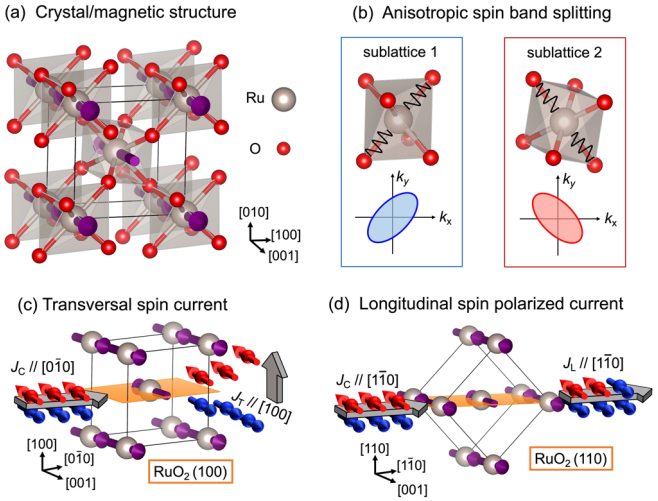

FIG. 1. (a) Crystal and magnetic structure of the rutile RuO_2. Gray and red spheres represent Ru and O atoms, respectively. Purple arrows mark the Ru local moments. (b) Schematic of the anisotropic spin band splitting in RuO_2. Oxygen octahedrons of two sublattices are rotated by 90°. The Ru atoms of two magnetic sublattices feel anisotropic octahedral crystal field (wavy black lines), leading to the anisotropic spin band splitting, as displayed by blue and red ellipses. (c) For the (100)-oriented RuO_2 film, transversal spin current (J_T) flowing along the [100] axis (out-of-plane) can be induced by the charge current along the [0$\bar{1}$0] axis. The spin polarization is parallel to the Néel vector ([001] axis). (d) For the (110)-oriented RuO_2 film, spin polarized current (J_L) flowing along longitudinal direction can be generated by the charge current along the [1$\bar{1}$0] axis. The spin polarization is also parallel to the Néel vector.

To probe SST experimentally, we deposited 12 nm thick (100)- and (110)-oriented RuO_2 films onto (100)-oriented yttria-stabilized zirconia (YSZ) and (100)-oriented MgO substrates, respectively. Then 8 nm thick ferromagnetic permalloy (Py) layer and 2 nm thick Al capping layer were *in situ* deposited on the RuO_2 films. After fabricating into the device, we performed spin torque-ferromagnetic resonance (ST-FMR) measurements [25], which is a standard technique to detect spin current and spin torque. Note that ST-FMR is widely used to calibrate the spin current strength and distinguish the spin polarization direction [18,20,21,26], which makes it pretty suitable for detecting SST. Compared to other detection techniques of charge-to-spin conversion, such as the harmonic Hall measurement, ST-FMR has the advantage of simplicity and large signal intensity [35]. In this work, two key parameters (spin torque efficiency θ_{SH}^{eff} and spin torque conductivity σ_{SH}^{eff}) are extracted from the ST-FMR signals to calibrate the charge-to-spin conversion efficiency. Herein, θ_{SH}^{eff} refers to the spin current density per unit current density, and σ_{SH}^{eff} represents the angular momentum absorbed by the magnet per second per unit interface area per applied electric field. The detailed analysis methods of the ST-FMR signals are presented in the Supplemental Material [25].

Then we turn to the experimental results. We show in Figs. 2(c) and 2(d) the ST-FMR spectra of RuO_2/Py samples measured at $\varphi = 45°$, which can be decomposed into symmetric (V_S) and antisymmetric components (V_A). The angle between the charge current and the external magnetic field is termed as φ. Note that the rf current I_{rf} was estimated by calibrating the reflection coefficient (S_{11}) of the ST-FMR device, by which we conclude that V_A of the ST-FMR data mainly arises from the Oersted field [25]. As a result, the ratio of V_S/V_A is proportional to the spin torque efficiency [26]. Figure 2(c) displays the ST-FMR spectrum of the $RuO_2(100)$/Py sample. From first glance, the amplitude of V_S is comparable to V_A ($V_S/V_A = 0.36$), indicating the Py layer absorbs a strong spin torque [26]. The situation turns out to be dramatically different for the $RuO_2(110)$/Py, where the amplitude of V_S is much smaller than V_A ($V_S/V_A = 0.10$), implying weak spin torque exerting on

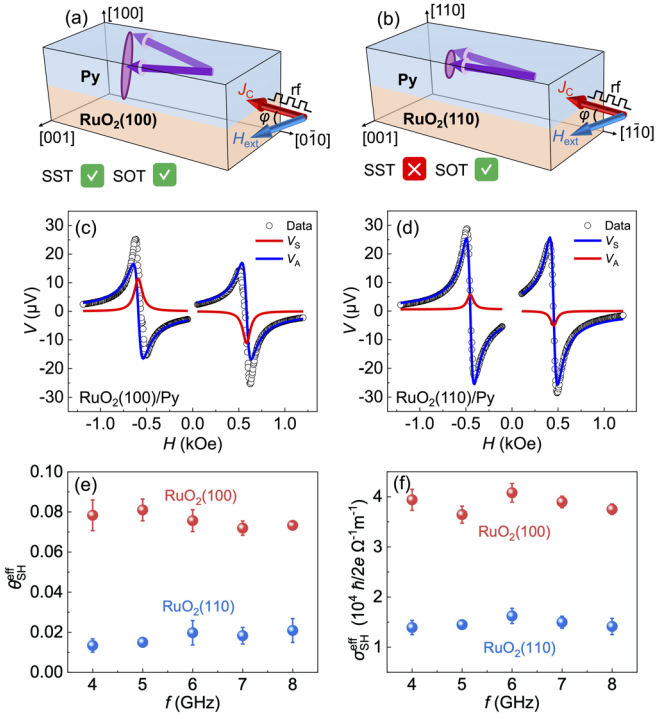

FIG. 2. (a),(b) Schematic of ST-FMR measurements for the (a) $RuO_2(100)$/Py and the (b) $RuO_2(110)$/Py samples. For the $RuO_2(100)$ film, both spin splitting torque (SST) and spin-orbit torque (SOT) exist, giving rise to a strong spin torque. For the $RuO_2(110)$ film, SST is absent, only SOT contributes to a weak spin torque. The angle between the charge current (J_C) and the external magnetic field (H_{ext}) is termed as φ. (c),(d) ST-FMR spectra of the (c) $RuO_2(100)$/Py and the (d) $RuO_2(110)$/Py samples measured at $\varphi = 45°$ and $f = 6$ GHz. The input power $P_{in} = 15$ dBm. Circles are the raw data; red and blue lines represent the symmetric (V_S) and the antisymmetric (V_A) components, respectively. (e),(f) The calculated (e) spin torque efficiency θ_{SH}^{eff} and the (f) spin torque conductivity σ_{SH}^{eff} at different microwave frequencies in $RuO_2(100)$ and $RuO_2(110)$ films. The error bars are from three repetitive measurements.

the Py layer, as displayed in Fig. 2(d). The angle-dependent ST-FMR measurements also draw the same conclusion [25]. We mention that this distinction shows the characteristic of SST, as shown in Figs. 2(a) and 2(b). For the $RuO_2(100)/Py$ sample, both SST and SOT exist, giving rise to strong resonance and large V_S/V_A ratio [Fig. 2(a)]. While for the $RuO_2(110)/Py$ sample, the SST is absent, only weak resonance and small V_S/V_A ratio are induced by SOT [Fig. 2(b)].

In order to quantitatively compare the spin torque efficiency of the two samples, θ_{SH}^{eff} is calculated by Eq. (S2) [25]. Corresponding data are shown in Fig. 2(e). For both (100)- and (110)-oriented RuO_2 films, θ_{SH}^{eff} exhibit little variation as a function of microwave frequency, excluding artifacts rooted from the specified microwave frequency. For the $RuO_2(100)$ film θ_{SH}^{eff} is about 0.08, which is much larger than that of $RuO_2(110)$ film ($\theta_{SH}^{eff} \sim 0.02$) and is comparable to that of the typical heavy metal Pt [26]. Similar crystal orientation-dependent θ_{SH}^{eff} was observed in rutile paramagnetic IrO_2 [36]. Furthermore, the effective spin torque conductivity (σ_{SH}^{eff}) is calculated for the two samples by estimating the rf current [25]. Corresponding data are plotted in Fig. 2(f). For the (100)-oriented RuO_2 film, σ_{SH}^{eff} is up to $4 \times 10^4\ \hbar/2e\,\Omega^{-1}\ m^{-1}$, which is around 3 times as large as that of the (110)-oriented RuO_2 film. Note that we calibrated the interfacial spin transparencies of these two samples by the ferromagnetic resonance measurement, the effective spin mixing conductance $g_{eff}^{\uparrow\downarrow}$ of them are comparable [25], thereby the enhanced spin torque efficiency in the $RuO_2(100)$ sample can be ascribed to an extra spin current generation mechanism in addition to SHE. The generation of SST due to the anisotropic spin band splitting is a reasonable explanation, which is also in agreement with the theoretical prediction [12].

To further investigate the SST in RuO_2, magnetic field annealing was carried out in the $RuO_2(100)/Py$ sample to align the Néel vector along the direction of the annealing field (H_{FA}) [25,27]. Subsequently, we performed φ-dependent ST-FMR measurements for the scenario of charge current (J_C) perpendicular, parallel, and at an angle β to H_{FA}, the results are shown in Fig. 3. For the case of $J_C \perp H_{FA}$, the angular dependence of V_S can be fitted by $\sim \sin 2\varphi \cos\varphi$ [Fig. 3(b)], indicating the major contribution from y-axis spin polarization (σ_y). This is supported by the line-shape separation result that the amplitude of $V_{y,DL}$ (blue line) is much larger than that of $V_{x,DL}$ (red line). The ratio of $|\theta_x^{eff}/\theta_y^{eff}|$ (equivalent to the $|V_{x,DL}/V_{y,DL}|$ [25]) is ~0.07 in this case. Here, σ_i represents the i-axis spin polarization, $V_{i,FL(DL)}$ refers to the voltage signal contributed by the fieldlike (dampinglike) torque of σ_i, θ_i^{eff} represents the spin torque efficiency of σ_i. The scenario differs dramatically when $J_C // H_{FA}$. Corresponding data in Fig. 3(d) are not inconsistent with the angular dependence $\sim \sin 2\varphi \cos\varphi$. By the fitting based on Eq. (S3) [25], it is found that the amplitude

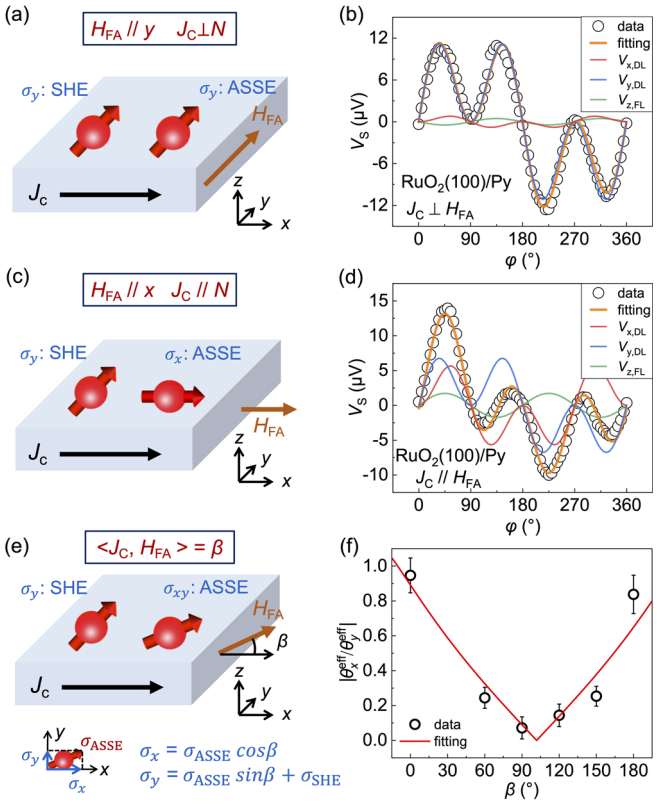

FIG. 3. (a),(c),(e) Schematic of spin current generation in (100)-oriented RuO_2 with (a) $J_C \perp H_{FA}$, (c) $J_C // H_{FA}$, or (e) $\langle J_C, H_{FA} \rangle = \beta$ (The angle between J_C and H_{FA} is β). J_C and H_{FA} represent the charge current and the annealing field, respectively. (b),(d) Angle-dependent V_S of ST-FMR data for configurations of (b) $J_C \perp H_{FA}$ and (d) $J_C // H_{FA}$. Orange lines are fitted by the Eq. (S3) [25]. Red, blue, and green lines represent angle-dependent voltage signals contributed by the dampinglike torque of σ_x, σ_y as well as the fieldlike torque of σ_z, respectively. σ_i represents the i-axis spin polarization. (f) Ratios of $|\theta_x^{eff}/\theta_y^{eff}|$ as a function of β. θ_i^{eff} represents the spin torque efficiency of σ_i. Red line is fitted by the expression of $|\cos\beta/(\sin\beta + C)|$. The specific positions of $J_C \perp H_{FA}$ and $J_C // H_{FA}$ for $\beta = 90°$ and 180°, respectively, are highlighted. The error bars are from three repetitive measurements.

of $V_{x,DL}$ is comparable to that of $V_{y,DL}$ ($|\theta_x^{eff}/\theta_y^{eff}|$ is ~0.84), revealing that obvious x-axis spin polarization (σ_x) emerges. The results above are consistent with SST that spin polarization direction is parallel to the Néel vector, as depicted by the schematics in Figs. 3(a) and 3(c). In the case of $J_C \perp H_{FA}$, both SHE and ASSE induced spins are along the y axis, and σ_x is absent. While for the scenario of the $J_C // H_{FA}$, σ_x is generated by the ASSE.

When the charge current is at an angle β to H_{FA}, spin polarization generated by ASSE has both x-axis and y-axis components [Fig. 3(e)], giving rise to a β-dependent ratio of $\theta_x^{eff}/\theta_y^{eff}$. As analyzed in Fig. S16, $|\theta_x^{eff}/\theta_y^{eff}| \sim |\cos\beta/(\sin\beta + C)|$, where the constant C represents the ratio of $\theta_{SHE}^{eff}/\theta_{ASSE}^{eff}$ [25]. Here, θ_{SHE}^{eff} and θ_{ASSE}^{eff} represent the spin torque efficiency induced by SHE and ASSE,

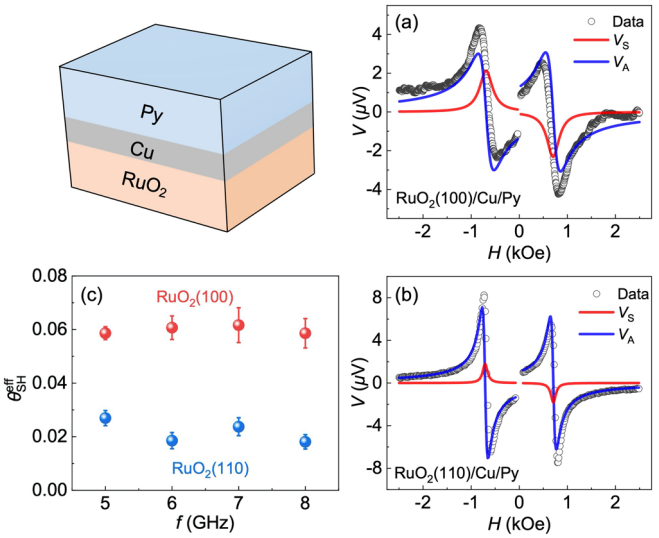

FIG. 4. ST-FMR measurement results for the samples with 2 nm thick Cu insertion. (a),(b) ST-FMR spectra of (a) $RuO_2(100)$/Cu/Py and (b) $RuO_2(110)$/Cu/Py samples. Red and blue lines are the symmetric (V_S) and the antisymmetric (V_A) components. (c) Calculated θ_{SH}^{eff} at different microwave frequencies for the $RuO_2(100)$/Cu/Py and the $RuO_2(110)$/Cu/Py samples.

respectively. We plot in Fig. 3(f) the experimental ratios of $|\theta_x^{eff}/\theta_y^{eff}|$ at different β, which can be well fitted by the equation above. This result further supports the conclusion that SST exists in $RuO_2(100)$ films. The minimum of the fitting line deviates slightly from 90°, which is ascribed to the fitting error and the angle error in the device fabrication. Note that the $V_{z,FL}$ term with angular dependence $\sim \sin 2\varphi$ (green line) appears in Fig. 3(d), which could originate from the spin precession [19–21,37]. Angle-dependent ST-FMR measurements were also carried out in the $RuO_2(110)$/Py sample with magnetic field annealing. In this case, σ_x is negligible, which is consistent with the theoretical analysis [12,25].

Besides SST, magnetic moment-dependent spin torque behaviors can be induced by the magnetic (antiferromagnetic) spin Hall effect (MSHE or AFM-SHE), where the interfacial effect (e.g., interfacial spin precession) plays a key role [19,21,38–41]. Differently, the origin of the $\mathcal{T}$-odd SST is ascribed to the SOC-independent magnetic exchange interaction, where the bulk contribution is dominant. To exclude the influence of the interfacial effect, we show in Fig. 4 the ST-FMR data of RuO_2(12 nm)/Cu(2 nm)/Py(8 nm) samples. As presented in Figs. 4(a) and 4(b), the V_S/V_A ratio in the (100)-oriented RuO_2 sample is much larger than that of the (110)-oriented one, indicating the spin torque efficiency of the former is larger than that of the latter. The calculated θ_{SH}^{eff} at different frequencies are displayed in Fig. 4(c), which exhibit weak dependence on microwave frequency for both samples. θ_{SH}^{eff} of $RuO_2(100)$/Cu/Py sample is about 0.06, much larger than that of the $RuO_2(110)$/Cu/Py sample ($\theta_{SH}^{eff} \sim 0.02$), which demonstrates that the RuO_2 bulk dominates the generation of SST. This conclusion is supported by the angle-dependent ST-FMR measurements [25]. We point out that the slight reduction of θ_{SH}^{eff} compared to the counterpart without Cu insertion is reasonable because the additional interface and Cu spacer may increase the spin loss.

Based on the clues described above (i.e., crystal orientation dependent spin torque efficiency, Néel vector dependent spin polarization direction and bulk dominant contribution), we claim that SST is observed in the $RuO_2(100)$/Py sample. Then we tend to compare the present ASSE and previous AFM-SHE [21]. Phenomenologically, ASSE-induced spin current generation in antiferromagnetic RuO_2 is the AFM-SHE-like behavior, because both of them show Néel vector dependent charge-spin conversion. Nevertheless, strictly speaking, ASSE in RuO_2 is different from AFM-SHE because the former is dependent on nonrelativistic crystal structure (spin band) rather than the relativistic spin-orbit coupling.

Apart from the controllable spin polarization, SST in RuO_2 brings about ultrahigh spin torque conductivity, making it a promising spin source in spintronics. Combining the predicted ultrahigh charge-spin conversion efficiency [12] and ultralow resistivity measured in single crystal [42], the maximum σ_{SH}^{eff} of $RuO_2(100)$ is as high as $8 \times 10^5\ \hbar/2e\,\Omega^{-1}\,m^{-1}$, which is larger than that of typical heavy metals and topological insulators, e.g., Pt $\sim 3.4 \times 10^5$, β-Ta $\sim 8 \times 10^4$, and $Bi_2Se_3 \sim 2 \times 10^5\ \hbar/2e\,\Omega^{-1}\,m^{-1}$ [7,26,43]. Such a large value is ascribed to the nonrelativistic anisotropic spin splitting effect. In addition, some other interesting physical behaviors including the crystal Hall effect [44,45], the giant tunneling magnetoresistance [46,47], the strain-induced superconductivity [48,49], as well as the spin-valley locking [50] were predicted theoretically or reported experimentally in rutile RuO_2. All these intriguing findings make RuO_2 an emergent material in condensed matter physics.

In summary, we provide experimental evidences for the observation of spin splitting torque in a collinear antiferromagnet RuO_2, where three typical features of SST were observed: (i) spin torque efficiency of $RuO_2(100)$ film is much larger than that of $RuO_2(110)$ film, because of the crystal orientation-dependent spin current flowing along the [100] axis of RuO_2; (ii) the direction of spin polarization generated by the $RuO_2(100)$ film is dependent on (parallel to) the Néel vector of RuO_2; and (iii) spin torque efficiencies measured in $RuO_2(100)$/Py samples with and without Cu insertion are comparable, and both are larger than that of $RuO_2(110)$ samples, demonstrating the bulk contribution is dominant. Spin splitting torque in RuO_2 brings about controllable spin polarization combined with ultrahigh spin torque conductivity, which makes RuO_2 a promising spin source in spintronics.

This work is supported by the National Key R&D Program of China (Grant No. 2021YFB3601301), the National Natural Science Foundation of China (Grant No. 51871130) and and the Natural Science Foundation of Beijing, China (Grant No. JQ20010). C. S. acknowledges the support of Beijing Innovation Center for Future Chip (ICFC), Tsinghua University.

Note added.—After finishing the experimental work and during the manuscript preparation, we are aware of a relevant work that demonstrated (101)-oriented RuO_2 can generate out-of-plane spin polarization [28]. In this work, we mainly focus on the spin splitting torque generated in (100)-oriented RuO_2.

*These authors contributed equally to this work.
†Corresponding author.
fanxiaolong@lzu.edu.cn
‡Corresponding author.
songcheng@mail.tsinghua.edu.cn

[1] L. Berger, Emission of spin waves by a magnetic multilayer traversed by a current, Phys. Rev. B **54**, 9353 (1996).
[2] J. C. Slonczewski, Current-driven excitation of magnetic multilayers, J. Magn. Magn. Mater. **159**, L1 (1996).
[3] J. A. Katine, F. J. Albert, R. A. Buhrman, E. B. Myers, and D. C. Ralph, Current-Driven Magnetization Reversal and Spin-Wave Excitations in Co/Cu/Co Pillars, Phys. Rev. Lett. **84**, 3149 (2000).
[4] A. Brataas, A. D. Kent, and H. Ohno, Current-induced torques in magnetic materials, Nat. Mater. **11**, 372 (2012).
[5] D. Apalkov, A. Khvalkovskiy, S. Watts, V. Nikitin, X. Tang, D. Lottis, K. Moon, X. Luo, E. Chen, A. Ong, A. Driskill-Smith, and M. Krounbi, Spin-transfer torque magnetic random access memory (STT-MRAM), ACM J. Emerg. Technol. Comput. Syst. **9**, 1 (2013).
[6] I. M. Miron, K. Garello, G. Gaudin, P. J. Zermatten, M. V. Costache, S. Auffret, S. Bandiera, B. Rodmacq, A. Schuhl, and P. Gambardella, Perpendicular switching of a single ferromagnetic layer induced by in-plane current injection, Nature (London) **476**, 189 (2011).
[7] L. Liu, C. F. Pai, Y. Li, H. W. Tseng, D. C. Ralph, and R. A. Buhrman, Spin-torque switching with the giant spin Hall effect of tantalum, Science **336**, 555 (2012).
[8] L. Liu, O. J. Lee, T. J. Gudmundsen, D. C. Ralph, and R. A. Buhrman, Current-Induced Switching of Perpendicularly Magnetized Magnetic Layers Using Spin Torque from the Spin Hall Effect, Phys. Rev. Lett. **109**, 096602 (2012).
[9] A. Manchon, J. Železný, I. M. Miron, T. Jungwirth, J. Sinova, A. Thiaville, K. Garello, and P. Gambardella, Current-induced spin-orbit torques in ferromagnetic and antiferromagnetic systems, Rev. Mod. Phys. **91**, 035004 (2019).
[10] C. Song, R. Zhang, L. Liao, Y. Zhou, X. Zhou, R. Chen, Y. You, X. Chen, and F. Pan, Spin-orbit torques: Materials, mechanisms, performances, and potential applications, Prog. Mater. Sci. **118**, 100761 (2021).
[11] M. Naka, S. Hayami, H. Kusunose, Y. Yanagi, Y. Motome, and H. Seo, Spin current generation in organic antiferromagnets, Nat. Commun. **10**, 4305 (2019).
[12] R. González-Hernández, L. Šmejkal, K. Výborný, Y. Yahagi, J. Sinova, T. Jungwirth, and J. Železný, Efficient Electrical Spin Splitter Based on Nonrelativistic Collinear Antiferromagnetism, Phys. Rev. Lett. **126**, 127701 (2021).
[13] M. Naka, Y. Motome, and H. Seo, Perovskite as a spin current generator, Phys. Rev. B **103**, 125114 (2021).
[14] K. H. Ahn, A. Hariki, K. W. Lee, and J. Kuneš, Antiferromagnetism in RuO_2 as d -wave Pomeranchuk instability, Phys. Rev. B **99**, 184432 (2019).
[15] L. D. Yuan, Z. Wang, J. W. Luo, E. I. Rashba, and A. Zunger, Giant momentum-dependent spin splitting in centrosymmetric low-Z antiferromagnets, Phys. Rev. B **102**, 014422 (2020).
[16] S. Hayami, Y. Yanagi, and H. Kusunose, Bottom-up design of spin-split and reshaped electronic band structures in antiferromagnets without spin-orbit coupling: Procedure on the basis of augmented multipoles, Phys. Rev. B **102**, 144441 (2020).
[17] L. D. Yuan, Z. Wang, J. W. Luo, and A. Zunger, Strong influence of nonmagnetic ligands on the momentum-dependent spin splitting in antiferromagnets, Phys. Rev. B **103**, 224410 (2021).
[18] D. Macneill, G. M. Stiehl, M. H. D. Guimaraes, R. A. Buhrman, J. Park, and D. C. Ralph, Control of spin–orbit torques through crystal symmetry in WTe_2/Ferromagnet bilayers, Nat. Phys. **13**, 300 (2017).
[19] S. H. C. Baek, V. P. Amin, Y. W. Oh, G. Go, S. J. Lee, G. H. Lee, K. J. Kim, M. D. Stiles, B. G. Park, and K. J. Lee, Spin currents and spin-orbit torques in ferromagnetic trilayers, Nat. Mater. **17**, 509 (2018).
[20] T. Nan *et al.*, Controlling spin current polarization through non-collinear antiferromagnetism, Nat. Commun. **11**, 4671 (2020).
[21] X. Chen, S. Shi, G. Shi, X. Fan, C. Song, X. Zhou, H. Bai, L. Liao, Y. Zhou, H. Zhang, A. Li, Y. Chen, X. Han, S. Jiang, Z. Zhu, H. Wu, X. Wang, D. Xue, H. Yang, and F. Pan, Observation of the antiferromagnetic Spin Hall effect, Nat. Mater. **20**, 800 (2021).
[22] T. Berlijn, P. C. Snijders, O. Delaire, H. D. Zhou, T. A. Maier, H. B. Cao, S. X. Chi, M. Matsuda, Y. Wang, M. R. Koehler, P. R. C. Kent, and H. H. Weitering, Itinerant Antiferromagnetism in RuO_2, Phys. Rev. Lett. **118**, 077201 (2017).
[23] Z. H. Zhu, J. Strempfer, R. R. Rao, C. A. Occhialini, J. Pelliciari, Y. Choi, T. Kawaguchi, H. You, J. F. Mitchell, Y. Shao-Horn, and R. Comin, Anomalous Antiferromagnetism in Metallic RuO_2 Determined by Resonant X-Ray Scattering, Phys. Rev. Lett. **122**, 017202 (2019).
[24] L. F. Mattheiss, Electronic structure of RuO_2, OsO_2, and IrO_2, Phys. Rev. B **13**, 2433 (1976).
[25] See Supplemental Material at http://link.aps.org/supplemental/10.1103/PhysRevLett.128.197202 for the analysis of spin current from the anisotropic spin band splitting, sample preparation, and characterizations; ST-FMR devices and setup; detailed analysis method of the ST-FMR signal; the calibration of RF current and

Oersted field; frequency-dependent FMR measurements; data of angle-dependent ST-FMR measurements; key values of ST-FMR data in Figs. 2 and 4; detailed analysis of SST in $RuO_2(100)$/Py sample; and the comparison of ASSE and AFM-SHE, which includes Refs. [12,17,18,21,26–34].

[26] L. Liu, T. Moriyama, D. C. Ralph, and R. A. Buhrman, Spin-Torque Ferromagnetic Resonance Induced by the Spin Hall Effect, Phys. Rev. Lett. **106**, 036601 (2011).

[27] Y. W. Oh, S. H. C. Baek, Y. M. Kim, H. Y. Lee, K. D. Lee, C. G. Yang, E. S. Park, K. S. Lee, K. W. Kim, G. Go, J. R. Jeong, B. C. Min, H. W. Lee, K. J. Lee, and B. G. Park, Field-free switching of perpendicular magnetization through spin-orbit torque in antiferromagnet/ferromagnet/oxide structures, Nat. Nanotechnol. **11**, 878 (2016).

[28] A. Bose, N. J. Schreiber, R. Jain, D. Shao, H. P. Nair, J. Sun, X. S. Zhang, D. A. Muller, E. Y. Tsymbal, D. G. Schlom, and D. C. Ralph, Tilted spin current generated by the collinear antiferromagnet RuO_2, arXiv:2108.09150.

[29] Y. Wang, M. M. Decker, T. N. G. Meier, X. Chen, C. Song, T. Grünbaum, W. Zhao, J. Zhang, L. Chen, and C. H. Back, Spin pumping during the antiferromagnetic–ferromagnetic phase transition of iron–rhodium, Nat. Commun. **11**, 1 (2020).

[30] Y. C. Lau, D. Betto, K. Rode, J. M. D. Coey, and P. Stamenov, Spin-orbit torque switching without an external field using interlayer exchange coupling, Nat. Nanotechnol. **11**, 758 (2016).

[31] B. G. Park, J. Wunderlich, X. Martí, V. Holý, Y. Kurosaki, M. Yamada, H. Yamamoto, A. Nishide, J. Hayakawa, H. Takahashi, A. B. Shick, and T. Jungwirth, A spin-valve-like magnetoresistance of an antiferromagnet-based tunnel junction, Nat. Mater. **10**, 347 (2011).

[32] Y. Y. Wang, C. Song, B. Cui, G. Y. Wang, F. Zeng, and F. Pan, Room-Temperature Perpendicular Exchange Coupling and Tunneling Anisotropic Magnetoresistance in an Antiferromagnet-Based Tunnel Junction, Phys. Rev. Lett. **109**, 137201 (2012).

[33] S. Fukami, C. Zhang, S. Duttagupta, A. Kurenkov, and H. Ohno, Magnetization switching by spin-orbit torque in an antiferromagnet-ferromagnet bilayer system, Nat. Mater. **15**, 535 (2016).

[34] X. Marti, I. Fina, C. Frontera, J. Liu, P. Wadley, Q. He, R. J. Paull, J. D. Clarkson, J. Kudrnovský, I. Turek, J. Kuneš, D. Yi, J. H. Chu, C. T. Nelson, L. You, E. Arenholz, S. Salahuddin, J. Fontcuberta, T. Jungwirth, and R. Ramesh, Room-temperature antiferromagnetic memory resistor, Nat. Mater. **13**, 367 (2014).

[35] M. Nguyen and C. Pai, Spin–orbit torque characterization in a nutshell spin–orbit torque characterization in a nutshell, APL Mater. **9**, 030902 (2021).

[36] A. Bose, J. N. Nelson, X. S. Zhang, P. Jadaun, R. Jain, D. G. Schlom, D. C. Ralph, D. A. Muller, K. M. Shen, and R. A. Buhrman, Effects of anisotropic strain on spin-orbit torque produced by the dirac nodal line semimetal IrO_2, ACS Appl. Mater. Interfaces **12**, 55411 (2020).

[37] Y. You, H. Bai, X. Feng, X. Fan, L. Han, X. Zhou, Y. Zhou, R. Zhang, T. Chen, F. Pan, and C. Song, Cluster magnetic octupole induced out-of-plane spin polarization in antiperovskite antiferromagnet, Nat. Commun. **12**, 6524 (2021).

[38] M. Kimata, H. Chen, K. Kondou, S. Sugimoto, P. K. Muduli, M. Ikhlas, Y. Omori, T. Tomita, A. H. MacDonald, S. Nakatsuji, and Y. Otani, Magnetic and magnetic inverse spin Hall effects in a non-collinear antiferromagnet, Nature (London) **565**, 627 (2019).

[39] A. Mook, R. R. Neumann, A. Johansson, J. Henk, and I. Mertig, Origin of the magnetic spin Hall effect: Spin current vorticity in the Fermi sea, Phys. Rev. Research **2**, 023065 (2020).

[40] V. P. Amin and M. D. Stiles, Spin transport at interfaces with spin-orbit coupling: Formalism, Phys. Rev. B **94**, 104419 (2016).

[41] V. P. Amin and M. D. Stiles, Spin transport at interfaces with spin-orbit coupling: Phenomenology, Phys. Rev. B **94**, 104420 (2016).

[42] W. D. Ryden, A. W. Lawson, and C. C. Sartain, Electrical transport properties of IrO_2 and RuO_2, Phys. Rev. B **1**, 1494 (1970).

[43] A. R. Mellnik, J. S. Lee, A. Richardella, J. L. Grab, P. J. Mintun, M. H. Fischer, A. Vaezi, A. Manchon, E. A. Kim, N. Samarth, and D. C. Ralph, Spin-transfer torque generated by a topological insulator, Nature (London) **511**, 449 (2014).

[44] L. Šmejkal, R. González-Hernández, T. Jungwirth, and J. Sinova, Crystal time-reversal symmetry breaking and spontaneous Hall effect in collinear antiferromagnets, Sci. Adv. **6**, eaaz8809 (2020).

[45] Z. Feng, X. Zhou, L. Šmejkal, L. Wu, Z. Zhu, H. Guo, R. González-Hernández, X. Wang, H. Yan, P. Qin, X. Zhang, H. Wu, H. Chen, Z. Xia, C. Jiang, M. Coey, J. Sinova, T. Jungwirth, and Z. Liu, Observation of the crystal Hall effect in a collinear antiferromagnet, arXiv:2002.08712.

[46] L. Šmejkal, A. B. Hellenes, R. González-Hernández, J. Sinova, S. Nakatsuji, and T. Jungwirth, Giant and Tunneling Magnetoresistance in Unconventional Collinear Antiferromagnets with Nonrelativistic Spin-Momentum Coupling, Phys. Rev. X **12**, 011028 (2022).

[47] D.-F. Shao, S.-H. Zhang, M. Li, and E. Y. Tsymbal, Spin-neutral currents for spintronics, Nat. Commun. **12**, 7061 (2021).

[48] M. Uchida, T. Nomoto, M. Musashi, R. Arita, and M. Kawasaki, Superconductivity in Uniquely Strained RuO_2 Films, Phys. Rev. Lett. **125**, 147001 (2020).

[49] J. P. Ruf, H. Paik, N. J. Schreiber, H. P. Nair, L. Miao, J. K. Kawasaki, J. N. Nelson, B. D. Faeth, Y. Lee, B. H. Goodge, B. Pamuk, C. J. Fennie, L. F. Kourkoutis, D. G. Schlom, and K. M. Shen, Strain-stabilized superconductivity, Nat. Commun. **12**, 59 (2021).

[50] H. Y. Ma, M. Hu, N. Li, J. Liu, W. Yao, J. F. Jia, and J. Liu, Multifunctional antiferromagnetic materials with giant piezomagnetism and noncollinear spin current, Nat. Commun. **12**, 2846 (2021).